



Tumor microenvironment-activated self-charge-generable metallosupramolecular polymer nanocapsules for photoacoustic imaging-guided targeted synergistic photothermal-chemotherapy

Jie Mao^{a,b,f,1}, Yang Li^{c,d,1}, Qipeng Cai^{a,b}, Zhenbin Tang^{a,b}, Yuxin Yang^{a,b}, Conghui Yuan^{a,b,*}, Yiting Xu^{a,b}, Birong Zeng^{a,b}, Weiang Luo^{a,b}, Shiaowei Kuo^e, Lizong Dai^{a,b,*}

^a College of Materials, Xiamen University, Xiamen 361005, PR China

^b Fujian Provincial Key Laboratory of Fire Retardant Materials, Xiamen University, Xiamen 361005, PR China

^c Fujian Institute of Research on the Structure of Matter, Chinese Academy of Sciences, Fuzhou 350002, PR China

^d Department of Translational Medicine, Xiamen Institute of Rare Earth Materials, Chinese Academy of Sciences, Xiamen 361024, PR China

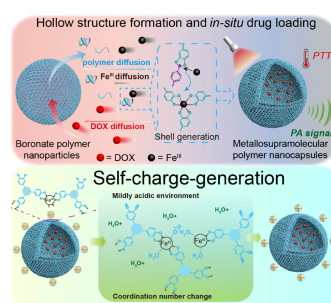
^e Department of Materials and Optoelectronic Science, Center for Supramolecular Materials and Functional Polymers, National Sun Yat-Sen University, Kaohsiung 804, Taiwan

^f School of Environment and Energy Engineering, Anhui Jianzhu University, Hefei 230601, PR China

HIGHLIGHTS

- Kirkendall effect in polymer system for the generation of hollow structure.
- Excellent photothermal and photoacoustic properties derived from TAC/Fe^{III} complex.
- Self-charge generation improves the circulation time and cellular uptake.

GRAPHICAL ABSTRACT



ARTICLE INFO

Keywords:

Tumor microenvironment
Self-charge-generation
Photothermal conversion
Photoacoustic imaging
Targeted photothermal-chemotherapy

ABSTRACT

An integrated nanosystem of target, visualization, high circulation stability, and multi-therapy effects represents the leading direction of next generation anti-cancer strategy. Nevertheless, this normally requires elegant multi-component and hierarchical structure design of nanomaterials, or even a complicated post-treatment procedure, to combine different functions together. Herein, we show that hollow metallosupramolecular polymer nanoparticles (HMPNs) derived from a selective-etching approach based on Kirkendall effect have combined capabilities of (i) facile *in-situ* guest cargo encapsulation, (ii) reversible surface charge evolution, (iii) excellent photoacoustic property and (vi) highly synergistic photothermal-chemo therapeutic effect. Using DOX as a model drug, we can easily fabricate DOX-HMPNs because the etching process is accompanied with effective matter exchange between outer environment and inner particle, while significantly avoiding the premature drug leakage. Notably, synergistic effect between reversible phenolic hydroxyl ionization and dynamic catechol-Fe^{III} coordination endows DOX-HMPNs with dramatic self-charge generation ability, thus achieving weakly acidic tumor microenvironment-activated reversible surface charge evolution. We have found that DOX-HMPNs with this self-charge generation feature can effectively achieve prolonged circulation and tumor recognition.

* Corresponding authors at: College of Materials, Xiamen University, Xiamen 361005, PR China.

E-mail addresses: yuanch@xmu.edu.cn (C. Yuan), lzdai@xmu.edu.cn (L. Dai).

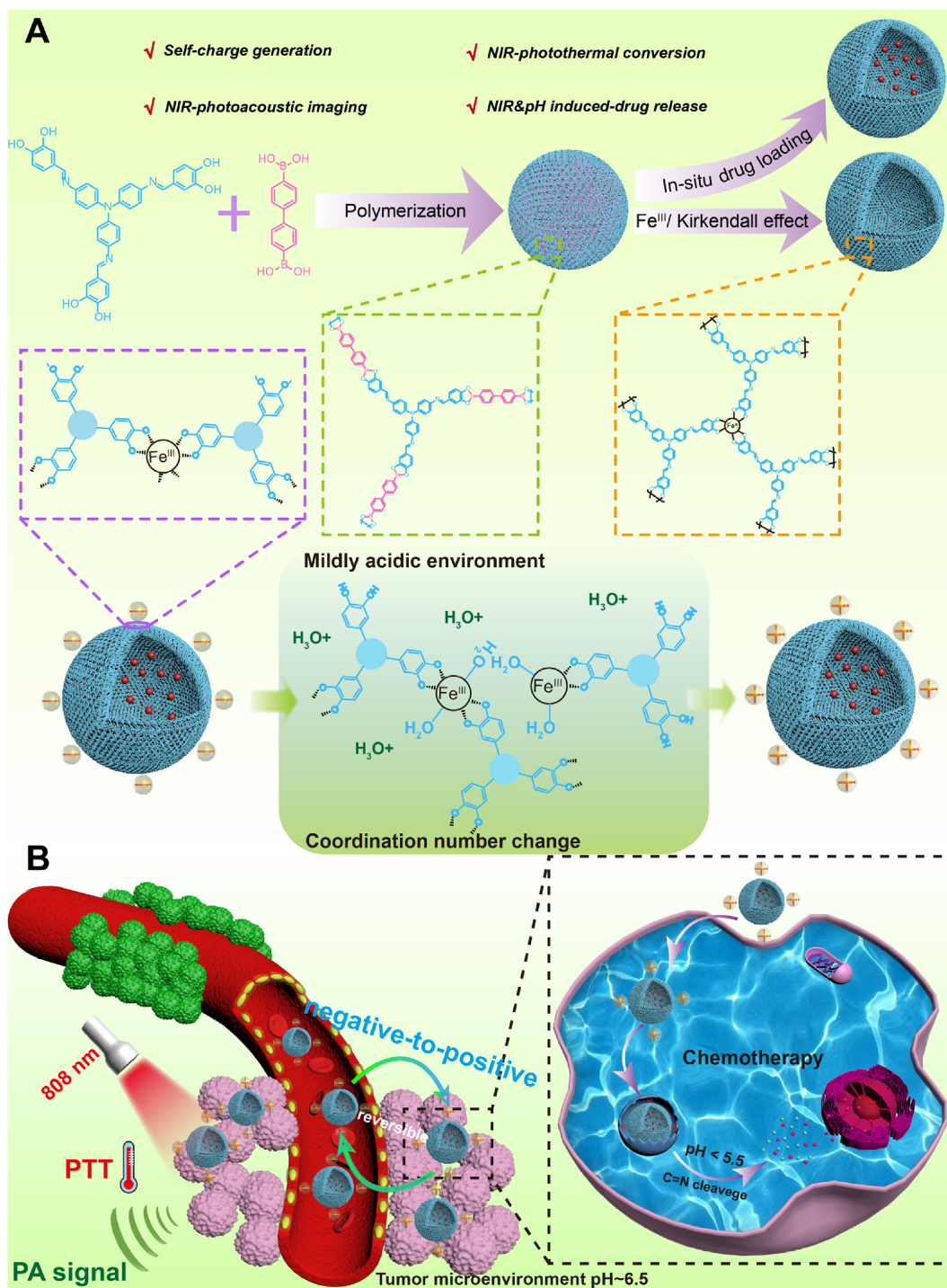
¹ J. Mao and Y. Li contributed equally to this work.

Moreover, the cleavage of imine bond can induce the disassembly of hollow particles in strongly acidic lysosomes, and thus accelerate the release of DOX. This chemotherapy, in combination with the cascade-responsive behavior and photothermal/photoacoustic properties of HMPNs, makes our DOX-HMPNs exhibit synergistic antitumor efficiency and provide promising potential for cancer theranostic application.

1. Introduction

Towards the targeting tumor diagnosis and therapy, nanosystems

with complicated composition and structure have shown irreplaceable advantages, as they can jointly achieve ostentatious superadditive therapeutic effect. [1–3] This type of nanosystem is normally



Scheme 1. (A) Schematic illustration of the preparation process of HMPNs, *in-situ* drug loading to form DOX-HMPNs, and tumor microenvironment-activated reversible “negative-to-positive” surface charge evolution. (B) Illustration of the photoacoustic imaging-guided targeted synergistic photothermal-chemotherapy of DOX-HMPNs.

constructed by guest cargo and nanocarrier. Particularly, the nanocarrier should be functional or smart, thus displaying high capability to manage the cargo, or even cooperate with the cargo to generate synergistic effects. [4–7] Among numerous nanocarriers, hollow nanoparticles are of particular interest for the achievement of synergistic therapy, because of their designable shell intrinsic properties and large interior void to accommodate guest cargoes. [8–11] Benefited from the rapid development of nanosynthesis, photothermal, [12–13] photodynamic and sonodynamic therapies, [14–16] have been realized in different shells. After introduction of guest cargoes such as drugs, immunologic adjuvants, imaging reagents and photosensitizers into these hollow nanoparticles, combined therapies such as chemo-photothermal therapy, [17–19] chemo-photodynamics therapy, [20] photodynamics-photothermal therapy [21–22] and imaging guided therapy [23–25] can be achieved. To further reinforce the diagnosis and therapy effects, the nanocarriers need to have a high tumor recognition ability. This can be achieved through a design of stimuli-responsive shell [26] or anchoring a targeting molecule on the shell surface. [27–28] Nevertheless,

it is still a great challenge to design hollow nanoparticles with both intrinsic diagnosis/therapy and stimuli-responsive properties.

Strategies such as self-assembly, [29–30] template-assistance, [31] Kirkendall effect, [32–33] Ostwald ripening, [34–35] Galvanic replacement, [36–37] and *etc.* have been widely adopted to create hollow nanoparticles with compositions ranging from polymers, lipoids, metals, metal oxides, to silicon dioxide. When these hollow nanoparticles are applied in biomedical area, the guest cargoes are normally loaded through a post-treatment procedure after the formation of hollow structure. This strategy is accompanied by many drawbacks including low encapsulation efficiency, easy guest leakage, complicated sealing procedure and so on. [9,17–18,20] Accordingly, it is highly desirable to exploit a highly facile and adaptable strategy to hollow nanoparticles, which can achieve in-situ guest cargo encapsulation during void formation.

In this work, we design a type of hollow metallosupramolecular polymer nanoparticles (HMPNs) with integrated functions of photothermal conversion, photoacoustic property, tumor microenvironment-

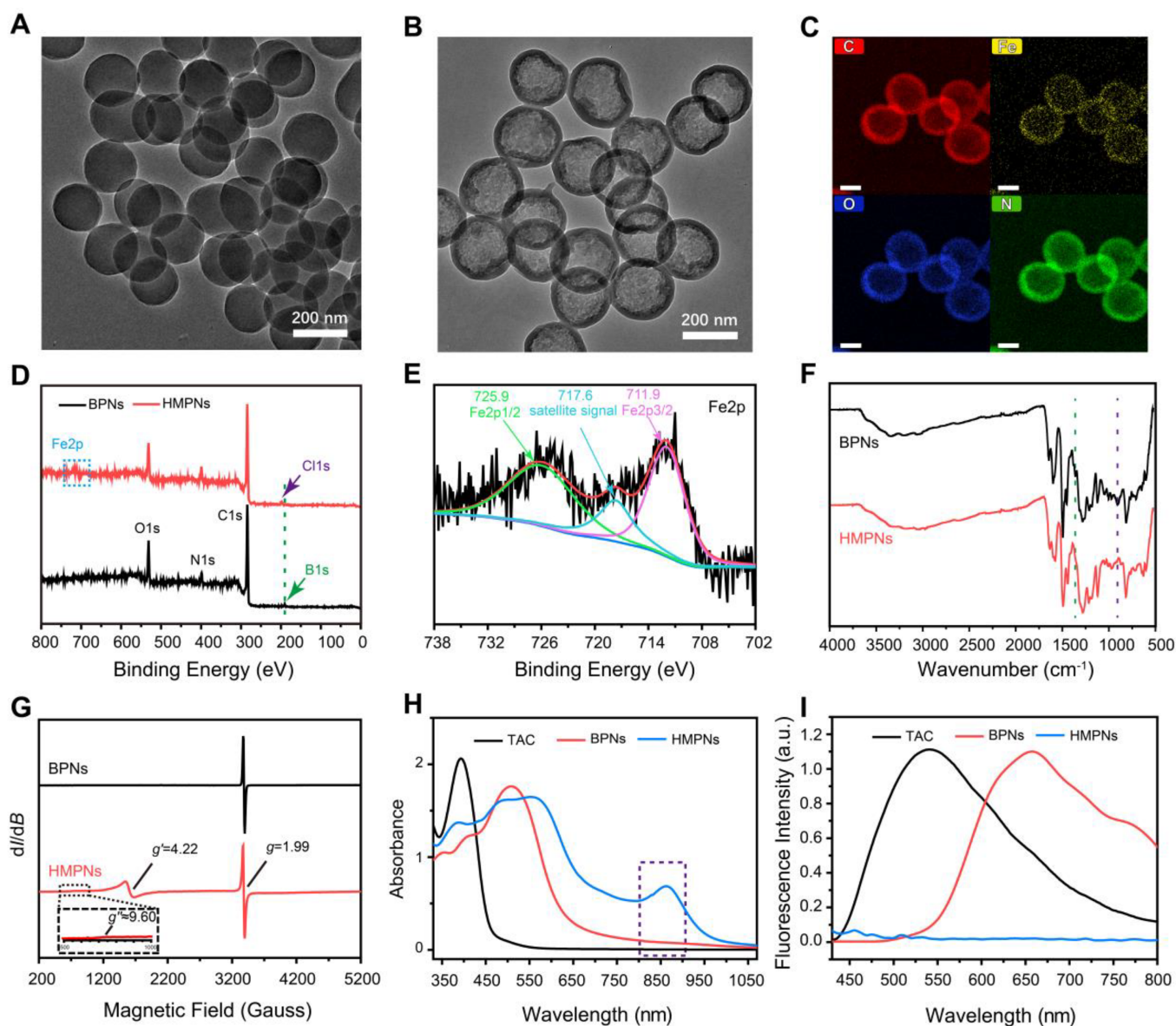


Fig. 1. (A, B) TEM image of (A) BPNs and (B) HMPNs. (C) EDX mapping of HMPNs (scale bar = 100 nm). (D) XPS survey spectra of BPNs and HMPNs. (E) High-resolution XPS spectrum of HMPNs (Fe2p region). (F) FT-IR spectra of BPNs and HMPNs. (G) X-band EPR spectra of BPNs and HMPNs. (H) UV-vis-NIR spectra of catechol monomer TAC, BPNs and HMPNs. (I) Fluorescent emission spectra of catechol monomer TAC, BPNs and HMPNs (Ex: 410 nm).

triggered self-charge generation and pH-responsive drug release, through an etching approach based on Kirkendall effect. Because the Kirkendall effect induced void formation process is accompanied by the matter exchange between outer environment and interior nanoparticle, guest molecules can be *in-situ* encapsulated during the creation of void. As shown in Scheme 1, our etching strategy adopts boronate polymer nanoparticles (BPNs,) as starting materials. We have already found that the condensation reaction between a catechol monomer (TAC) and a boronic monomer (DBB) is accompanied with the formation of B-N coordination, and thus leads to the assembly of boronate polymer into BPNs. [38–39] Fe^{III} can coordinate with catechol group and cut off the boronate polymer. Kirkendall effect occurs along with this coordination reaction, and boronic monomer leaves. Therefore, the shell of HMPNs is composed of TAC/ Fe^{III} complex, which shows excellent photothermal and photoacoustic properties in response to a near infrared region (NIR) stimulus. When doxorubicin (DOX) is present in the reaction mixture, it can be simultaneously encapsulated to afford DOX-HMPNs. This approach has high adaptability to various boronate polymer building blocks and easily control over the shell thickness.

The Fe^{III} -TAC complex can easily change the number of catechol ligands in respond to tumor microenvironment (TME). The balanced evolution between the exposure of unsaturated Fe^{III} (positive charge) and ionization of phenolic hydroxyl (negative charge), endows the HMPNs with “self-charge generation” property. Thus, HMPNs can

undergo reversible and recyclable “negative-to-positive” surface charge evolution. This is different from the mechanism of frequently reported “charge-reversal” behaviors relying on bond cleavage [26,40–41] or protonation [42–44] processes, which are irreversible or kinetically dependent. Once HMPNs flow back into the bloodstream from the tumor microenvironment, their surface will rapidly and effectively switch from positive to negative, therefore decreasing the immune recognition and RES capture. We show that with the aid of enhanced tumor accumulation, improved cellular uptake, and responsive drug release, highly efficient tumor elimination can be achieved by photothermal-chemotherapy under the precise guidance of PA imaging in one cycle of treatment while preventing the tumor recurrence.

2. Results and discussions

2.1. Characterization of HMPNs and DOX-HMPNs

Our study starts with preparation for HMPNs without drug loaded to test the feasibility of the Kirkendall effect based strategy. HMPNs were prepared from BPNs, which derived from a B-N coordination assisted condensation copolymerization of TAC and DBB monomers. Transmission electron microscopy (TEM) image of BPNs shown in Fig. 1A displays mono-dispersed nanospheres with diameters of ~ 200 nm, corresponding with the DLS data (Figure S1). Fe^{III} has a

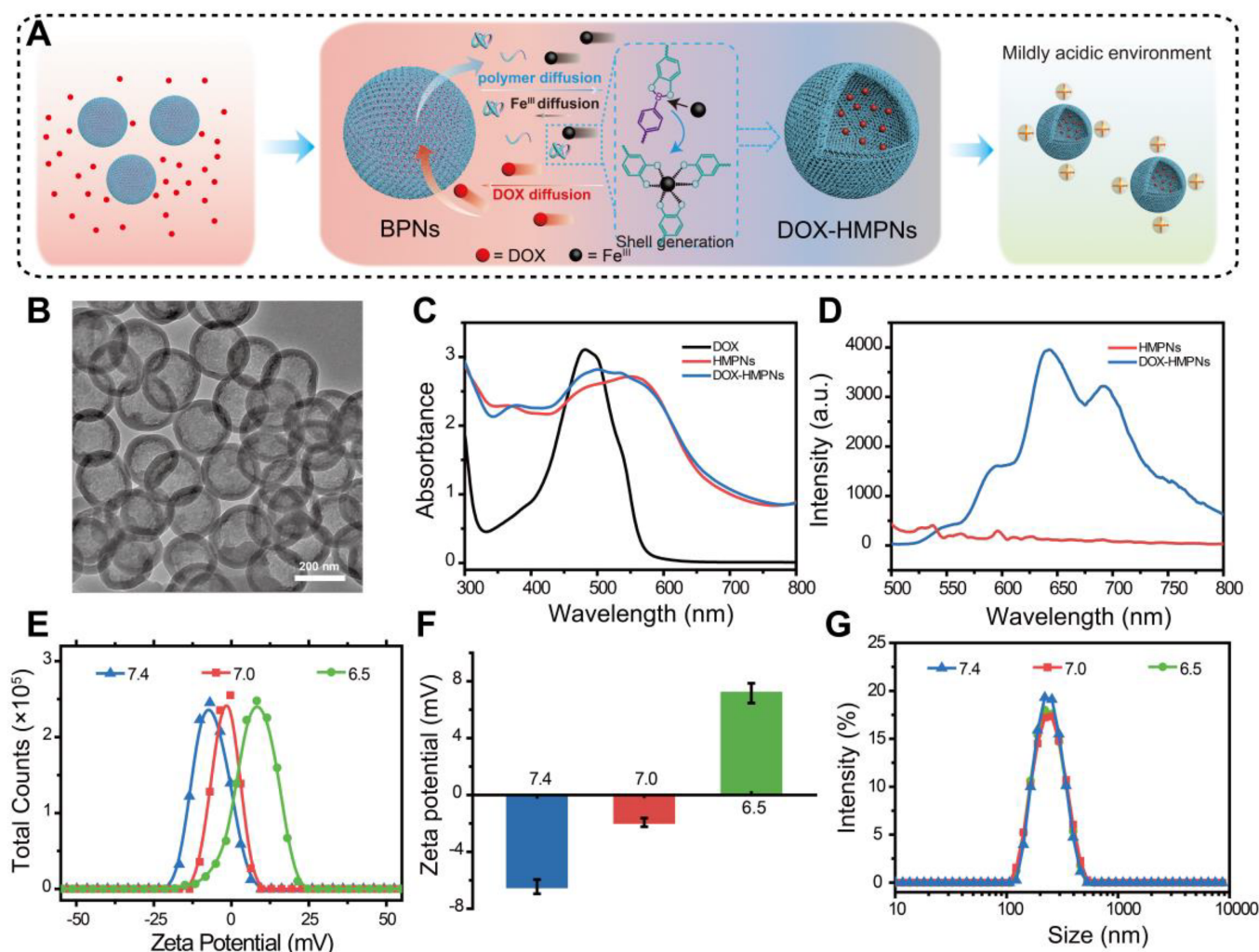


Fig. 2. (A) Illustration of Kirkendall effect based *in-situ* drug loading and mildly acidic environment induced charge reversal. (B) TEM image of DOX-HMPNs. (C) UV-vis spectra of DOX, HMPNs and DOX-HMPNs. (D) Fluorescent emission spectra of DOX-HMPNs and HMPNs (Ex: 480 nm). (E, F) Zeta potential of DOX-HMPNs after incubation at pH = 7.4, 7.0, and 6.5. (G) Size distribution of DOX-HMPNs at pH = 7.4, 7.0, and 6.5, respectively.

high binding affinity to catechol group, and the diffusion rate of Fe^{III} in the boronate polymer network is lower than the migration rate of boronate polymer chain from interior to the surface of BPNs. As a result, Fe^{III} can react with boronate polymer to induce the loss of boronic building block and create a TAC/ Fe^{III} metallosupramolecular polymer shell. This reaction process exhibits a typical feature of Kirkendall effect, as the hollow structure can only be formed at a relatively lower Fe^{III} . For example, HMPNs derived from 0.1 mmol/mL of Fe^{III} (the concentration of BPNs is kept at 1 mg/mL for all the syntheses of HMPNs) has shell thickness of ~ 25 nm (Fig. 1B), and the diameters has no significant difference with BPNs (Figure S1). By changing the concentration of Fe^{III} , the shell thickness of HMPNs can be tuned from 15 to 25 and 35 nm (Figure S2). The element mapping of HMPNs (Fig. 1C) confirms the hollow structure, and clearly reveals the homogeneous dispersion of four elements (C, N, O, and Fe) in the particle shell. In comparison, the element mapping of BPNs reveals the homogeneous

dispersion of four elements (C, N, O, B) (Figure S3).

X-ray photoelectron microscopy (XPS) analysis was performed to confirm the replacement of DBB by Fe^{III} and coordination between Fe^{III} and TAC. Compared to BPNs, the XPS survey spectrum of HMPNs (Fig. 1D) indicates the presence of Fe element and absent of B element. The O1s spectrum of BPNs (Figure S4) consists of signals at C-O (533.3 eV), B-O (532.0 eV), and C-OH (532.9 eV), implying that BPNs not only comprise boronate group, but also possess residual catechol and boronic functionalities. The O1s spectrum of HMPNs can be divided into two peaks at 531.4 eV and 532.9 eV, corresponding to the C-O-Fe and C-OH groups. [45–46] This result implies the coordination between Fe^{III} and TAC. The Fe2p spectrum of HMPNs in Fig. 1E shows two peaks centered at 711.9 and 725.9 eV, which are assigned to Fe^{III} 2p_{3/2} and Fe^{III} 2p_{1/2}, respectively. [47] In the FT-IR spectra, the characteristic peaks of B-O (1357 cm^{-1}) and C-B (900 cm^{-1}) stretching vibrations of boronate moiety can be easily identified to BPNs, while these signals

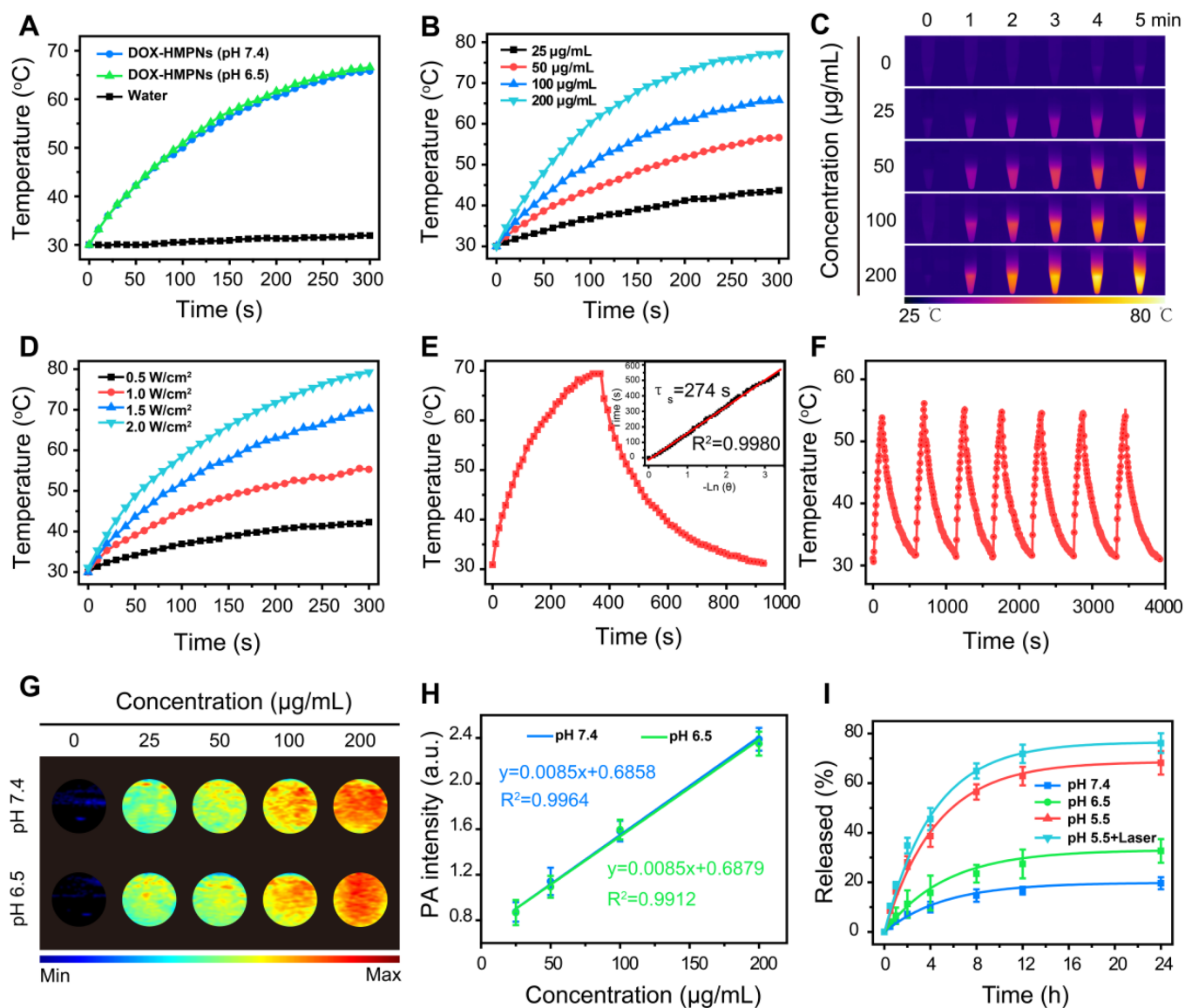


Fig. 3. (A) Photothermal heating curves of water and DOX-HMPNs at pH = 7.4 and 6.5 after 808 nm laser irradiation. Photothermal heating curves of DOX-HMPNs (B) with different concentrations and (C) corresponding infrared photothermal images. (D) Photothermal heating curves of DOX-HMPNs after 808 nm laser irradiation with different power densities. (E) Photothermal effect of DOX-HMPNs dispersions under laser irradiation (808 nm, 1.0 W cm^{-2}) and plot of cooling time versus negative natural logarithm of the temperature obtained from the cooling stage (inset). (F) Photothermal conversion of DOX-HMPNs during 7 times of on/off NIR irradiation cycles. (G) *In vitro* PA images of DOX-HMPNs with different concentrations at pH = 7.4 and 6.5 (808 nm laser). (H) Linear relationship between PA signal intensity and DOX-HMPNs concentration at pH = 7.4 and 6.5 ($n = 3$). (I) Cumulative release of DOX from DOX-HMPNs at $37\text{ }^\circ\text{C}$ at different pH values without/with 808 nm laser at pH = 5.5.

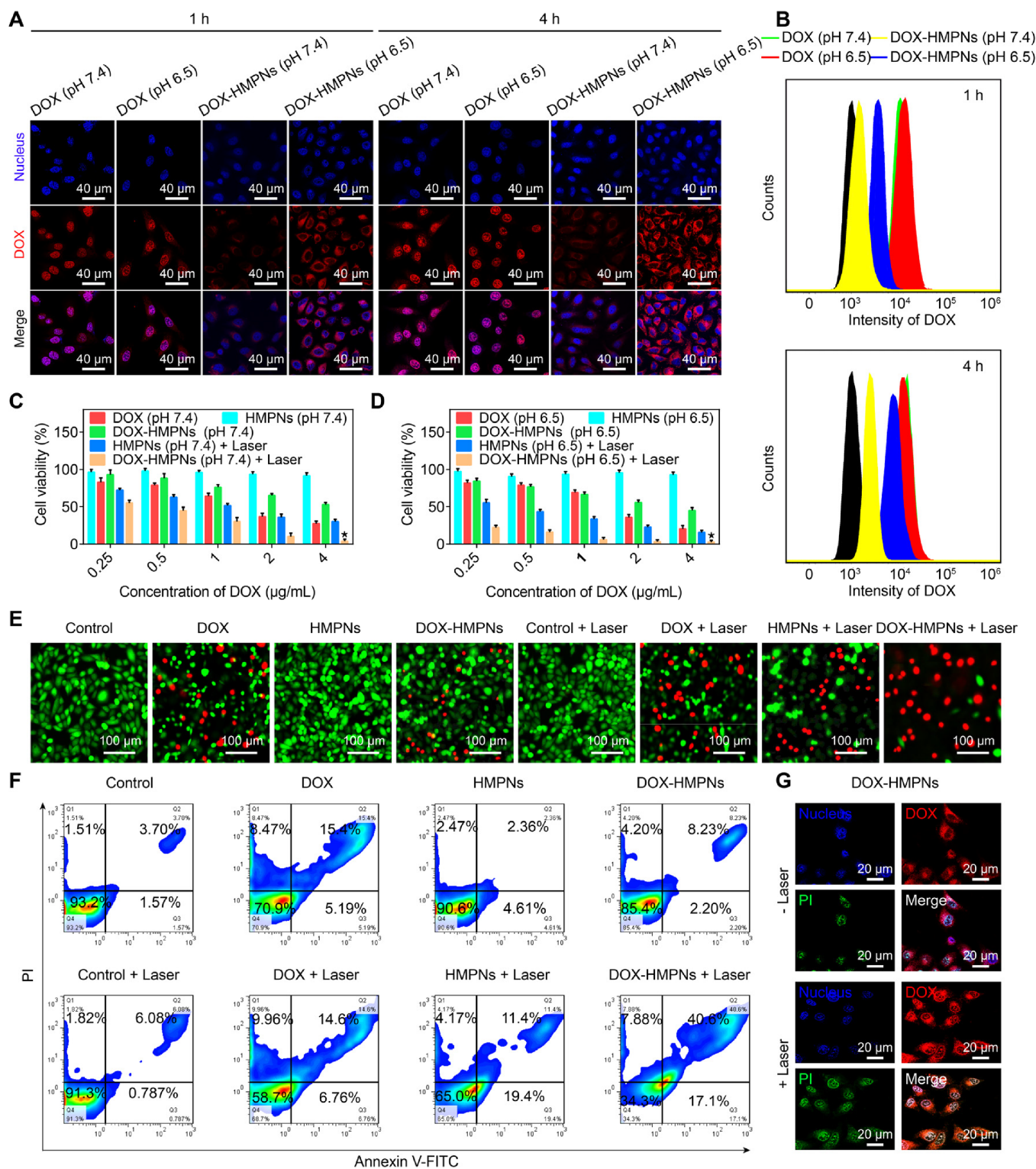


Fig. 4. (A) CLSM images and (B) flow cytometry profiles of MCF-7 cells incubated with free DOX and DOX-HMPNs at pH = 7.4 and 6.5 for 1 and 4 h. (C, D) Viability of MCF-7 cells treated with free DOX and DOX-HMPNs at (C) pH = 7.4 and (D) pH = 6.5 without/with laser irradiation (808 nm, 1 W cm⁻², 5 min) for 24 h incubation (n = 4). (E) CLSM images of live/dead staining of MCF-7 cells treated with different formulations without/with irradiation (808 nm, 1 W cm⁻², 5 min). (F) Cell apoptosis analysis via Annexin V-FITC/PI assay of MCF-7 cells treated with different formulations without/with laser irradiation (808 nm, 1 W cm⁻², 5 min) (n = 3). (G) CLSM images exhibiting the obvious apoptosis/necrosis of MCF-7 cells treated with DOX-HMPNs by combining laser irradiation. The cells were incubated with DOX-HMPNs (false-red fluorescence) for 1 h and then irradiated by laser for 5 min (808 nm, 1 W cm⁻²). After irradiation, the cells were further incubated for 30 min and stained with Hoechst 33,258 (false-blue fluorescence) and PI (false-green fluorescence). (For interpretation of the references to colour in this figure legend, the reader is referred to the web version of this article.)

disappear in the case of HMPNs (Fig. 1F), thus providing an additional indication for the cleavage of borate bond and loss of DBB. Electron paramagnetic resonance (EPR) spectroscopy was employed to probe of the number of catecholate coordinated to the Fe^{III} center (Fig. 1G). The EPR spectrum of BPNs only shows a sharp single at $g = 1.99$ which is ascribed to organic radical from catechol. However, the EPR spectrum of HMPNs displays a signal at $g' = 4.22$ with an additional weak edge resonance at $g'' \approx 9.60$, suggesting that the coordination of Fe^{III} with catechol and the Fe^{III} catecholate is in tri-coordination state. [48–49]

The UV-vis-NIR absorption and fluorescent emission tests were performed to compare the optical properties of TAC, BPNs and HMPNs. As shown in Fig. 1H, the UV-vis-NIR spectra of TAC and BPNs in EtOH displayed strong absorption peaks centered at ~ 395 and 510 nm. In contrast, the spectrum of HMPNs exhibit an obviously red shift absorption, with broadened absorption peaks at ~ 600 and 860 nm. Probably, the TAC/Fe^{III} coordination results in d-d electronic transition and expands the light absorption to NIR region. The fluorescent emission spectra of TAC and BPNs have maximum emissions at 540 nm and 660 nm under excitation at 410 nm. However, non-fluorescence emission is observed to HMPNs (Fig. 1I). Accordingly, the absorbed optical energy may be converted into heat instead of fluorescence emission. These excellent optical physical properties provide an opportunity for HMPNs to be used as a preminent theranostic nanoplatform. Hollow structure created through a Kirkendall effect strategy is accompanied with an efficient matter exchange between outer environment and interior nanoparticle. Therefore, we utilize this advantage to simultaneously load guest molecules during the void formation. Using DOX as a model drug, we can easily encapsulate DOX in interior of HMPNs to form DOX-HMPNs by simultaneously introducing Fe^{III} and DOX into a dispersion of BPNs (Fig. 2A). As shown in Fig. 2B, the DOX-HMPNs exhibit a similar morphology to HMPNs. The UV-vis absorption curves and fluorescence spectra confirmed the successful loading of DOX (Fig. 2C and D). The drug-loading capacity of the DOX-HMPNs was calculated to be $\sim 18.6\%$. Because of the residual catechol group can be ionized, both HMPNs and DOX-HMPNs exhibit negative surface charge. For example, as shown in Fig. 2E and F, DOX-HMPNs show strong negative charge (~ -6.45 mV) at $\text{pH} = 7.4$ (physiological condition). The TAC/Fe^{III} complex is dynamic, it can easily change from saturated to unsaturated coordination state in response to a weakly acidic environment, [50–51] thus leading to the exposure of Fe^{III} on the surface of the shell. With this self-charge generation capability, the original negative charge derived from catechol group is shielded. We have observed that DOX-HMPNs become electrically neutral (~ -1.93 mV) at $\text{pH} = 7.0$, and exhibit dramatic positive charge (~ -7.16 mV) up on decreasing the pH value to 6.5 (Fig. 2E and F), these results are similar to HMPNs (Figure S5). During the self-charge generation process, the diameter of nanoparticles exhibits no significant change (Fig. 2G). Notably, DOX-HMPNs display recyclable surface charge evolution and high cycle-stability (Figure S6), which may be of particular advantage in *in vivo* application.

2.2. Photothermal effect and photostability

The prominent absorbance of HMPNs at NIR region encouraged us to investigate the photothermal conversion performance of DOX-HMPNs. As depicted in the photothermal curves (Fig. 3A). Under an 808 nm NIR laser irradiation at a power density of 1 W cm^{-2} for 300 s, the temperature of a water dispersion of DOX-HMPNs with concentration of $100 \mu\text{g/mL}$ at $\text{pH} = 7.4$ swiftly increase to 65.8 °C. In contrast, no evident temperature increase can be observed to pure water under the same irradiation condition. Furthermore, no significant difference can be observed in the photothermal curves of DOX-HMPNs dispersed in water with $\text{pH} = 6.5$. This result indicates that a weak acidic environment has negligible influence on the photothermal performance of DOX-HMPNs. An increase of DOX-HMPNs concentration or a higher laser power density, can evidently improve the heating rate and final

temperature (Fig. 3B and D). The colors of thermal images (Fig. 3C) collected by the IR thermal camera are consistent with the results of photothermal curves.

To accurately evaluate the photothermal performance of DOX-HMPNs, the photothermal conversion efficiency (η) was assessed by the temperature decay curve of DOX-HMPNs dispersion (Fig. 3E), from which the η value of DOX-HMPNs was calculated to be 49% . This η value of HMPNs is higher than other photothermal agents in relevant literatures such as MoS₂ nanoparticles (37.5%), MOF-polydopamine hybrid nanogels (41.3%), liposomal indocyanine green (8.99%), gold nanovesicles (39%) and polypyrrole nanoparticles (44%) (Table S1, Supporting Information). Compared to metal nanoparticles, these hollow metallosupramolecular polymer nanoparticles demonstrate excellent biocompatibility and biodegradability, and have better photostability and photothermal conversion efficiency compared with small organic molecules such as ICG. Meanwhile, due to the large cavity of HMPNs, they exhibit outstanding transportation capacity in contrast with solid polymer nanoparticles. We then irradiated the suspension of DOX-HMPNs for 120 s with an 808 nm NIR laser, followed by switching off the laser and naturally cooling to room temperature. Notably, DOX-HMPNs can maintain its robust photothermal performance after seven cycles (Fig. 3F). Motivated by the excellent photothermal property, we envisaged that DOX-HMPNs might serve as photoacoustic (PA) contrast agent. Indeed, strong PA signal was detected for DOX-HMPNs at two different pH values under 808 nm irradiation (Fig. 3G). The PA intensity was evidently improved with the increase of particle concentration in a linear relationship ($R^2 = 0.9964$ and 0.9912) (Fig. 3H).

The drug release behavior of DOX-HMPNs was tested at various pH conditions with and without laser irradiation. As shown in Fig. 3I, the release of DOX from DOX-HMPNs reveals a typical photo-/pH-dependent manner. Cumulative drug releases of $\sim 20\%$ and $\sim 32\%$ are achieved within 24 h at $\text{pH} = 7.4$ and 6.5 , respectively. This value is dramatically increased to $\sim 68\%$ at $\text{pH} = 5.5$. Possibly, the acidic environment promotes the degradation of shell of the hollow particles through cleavage of imine bond, [52–54] thus facilitating the release of the encapsulated DOX. Under the irradiation of NIR laser, the cumulative release of DOX from DOX-HMPNs at $\text{pH} = 5.5$ is further increased to $\sim 76\%$ within 24 h. This is due to the local hyperthermia effect caused by the photothermal conversion of the shell, which can accelerate the diffusion of DOX from interior particle to the surrounding environment.

2.3. Cellular uptake and anticancer activity

To explore the cellular uptake of DOX-HMPNs, human breast carcinoma cell line MCF-7 cells were incubated with DOX-HMPNs for 1 and 4 h. In the confocal laser scanning microscopy (CLSM) images (Fig. 4A), the intensity of red fluorescence of DOX-HMPNs treated cells at $\text{pH} = 7.4$ and 6.5 is significantly weaker compared with that of free DOX treated cells after the same incubation time. This result can be explained by the fact that molecular DOX rapidly enters cells through a simple diffusion manner, whereas particle-like DOX-HMPNs are internalized by cells via slow endocytosis pathway (this will be further discussed below). Notably, the red fluorescence of DOX-HMPNs is dramatically enhanced when MCF-7 cells are exposed to weak acidity ($\text{pH} = 6.5$). The fluorescence intensity quantified by flow cytometer analysis supports the CLSM observation (Fig. 4B and S7). Accordingly, the tumor acidity-responsive self-charge generation of DOX-HMPNs, can enhance the cellular uptake of DOX-HMPNs at $\text{pH} = 6.5$.

The effect of NIR laser irradiation on the intracellular delivery of DOX-HMPNs after 4 h of incubation at $\text{pH} = 6.5$ is shown in Figure S8. Without irradiation treatment, the fluorescence signal is mainly distributed within the cytoplasm and perinuclear regions. In the case of NIR laser irradiation, strong red fluorescence signal (derived from DOX) is observed at the region of nucleus. Thus, NIR laser treatment can accelerate the intracellular drug release of DOX-HMPNs. Utilizing

LysoTracker Green DND-26 to identify lysosomes, we studied the sub-cellular distribution of DOX-HMPNs at pH = 6.5 after 4 h incubation. The effective overlap of red and green fluorescence signals (Figure S9), implies that the DOX-HMPNs were internalized by cells inside the lysosomes.

For biomedical application of nanomaterials, low toxicity or non-toxicity is very important. We thus assessed the dark toxicity of HMPNs against MCF-7 cells and murine breast carcinoma cell line 4 T1 cells via MTT assay. As shown in Fig. 4C and S10, the HMPNs exhibit no significant influence on the survival of MCF-7 and 4 T1 cells with viability above 90% after incubation for 24 h. This result was also observed on the normal cells including HUVES and L02 cells (Figure S11). These result indicated the biocompatibility of HMPNs. We further investigated the *in vitro* antitumor activity of DOX-HMPNs. With the presence of NIR laser irradiation, the photothermal-chemotherapy can be achieved to DOX-HMPNs. As evidenced in Figs. 4C, S12 and S13, delivery of DOX-HMPNs into MCF-7 cancer cells with NIR laser irradiation causes significant cytotoxicity. Control experiments performed without irradiation (chemotherapy alone), or without DOX (photothermal therapy alone), show evidently low cytotoxicity to cancer cells. Importantly, neither HMPNs nor NIR laser irradiation has notable cytotoxicity against MCF-7 cells (with viability of above 95%). For DOX-HMPNs at

DOX concentration of 1 $\mu\text{g}/\text{mL}$, more than 75% of MCF-7 cells are viable in the absence of irradiation, while only $\sim 30\%$ of cells are viable upon irradiation. This combined photothermal-chemotherapy is even more effective, when compared with HMPNs under irradiation (with viability of $\sim 52\%$), and free DOX with or without irradiation (with viability of $\sim 65\%$). In addition, the cytotoxicity of MCF-7 cells treated by DOX-HMPNs without irradiation, HMPNs with irradiation, and DOX-HMPNs with irradiation are significantly enhanced at pH = 6.5 compared to that at pH = 7.4, whereas this pH effect is not obvious in cases of DOX and HMPNs without irradiation (Fig. 4C, D). Similar results are also observed in 4 T1 cells (Figures S10 and S14). Accordingly, the self-charge generation capability of the DOX-HMPNs is effective in improving the photothermal-chemotherapy.

The result of calcein-AM/propidium iodide (PI) (live/dead) staining assay (Fig. 4E) is consistent very well with the result of MTT assay, confirming the significant cell-killing ability of DOX-HMPNs through photothermal-chemotherapy. Annexin V-FITC/PI apoptosis assay also reveals that DOX-HMPNs combined with NIR laser irradiation exhibits the highest apoptosis-inducing activity in comparison to the other groups (Fig. 4F, S15). Furthermore, the Hoechst 33258/PI staining assay confirms the results mentioned above (Fig. 4G). Thus, the photothermal-chemotherapy of DOX-HMPNs can remarkably enhance the

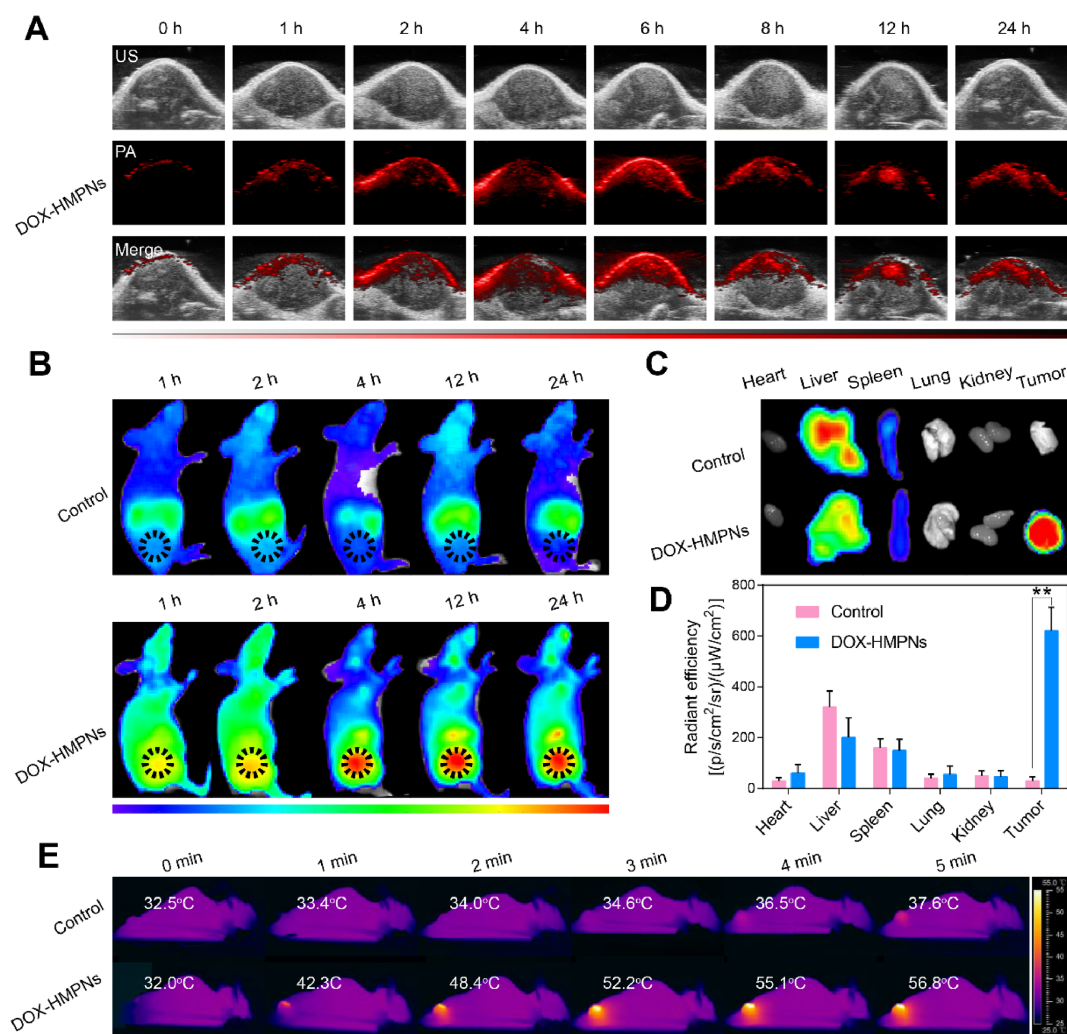


Fig. 5. (A) *In vivo* PA imaging of tumor areas of MCF-7 tumor-bearing mice after intravenous injection of DOX-HMPNs during 24 h. (B) *In vivo* NIR fluorescence imaging of MCF-7 tumor-bearing mice after intravenous injection of free Cy5 and DOX-HMPNs^{Cy5}. The tumors were indicated by the black circles. (C) *Ex vivo* NIR fluorescence imaging and (D) mean NIR fluorescence intensity of excised normal and tumor tissues ($n = 3$). Data were presented as mean \pm standard error. ** $P < 0.01$. (E) Infrared thermal imaging of MCF-7 tumor-bearing nude mice injected with PBS and DOX-HMPNs under NIR laser irradiation (808 nm, 1 W cm^{-2} , 5 min).

antitumor activity.

2.4. *In vivo* diagnosis and therapy

Prior to *in vivo* study, blood hemolysis test was carried out to study the blood compatibility of HMPNs and DOX-HMPNs. No obvious hemolysis is observed from blood treated with HMPNs and DOX-HMPNs at the highest concentration of $\sim 400 \mu\text{g mL}^{-1}$ for 4 h (Figure S16), suggesting the minimum damage of HMPNs and DOX-HMPNs against red blood cells and their excellent blood biocompatibility.

Encouraged by the intriguing PA property *in vitro*, the PA imaging *in vivo* was explored for precise tumor visualization, thus providing accurate information for targeted therapy. The PA imaging was performed using human breast tumor MCF-7-bearing BALB/c mice, and the PA images were obtained in a time-dependent method after intravenous administration of DOX-HMPNs *via* tail vein. The PA signals of DOX-HMPNs group can be easily detected in tumor regions at 0.5 h and gradually increased to maximum at 6 h, as verified in the semi-

quantitative analysis (Fig. 5A and S17). Then, the PA signals are slightly decreased at a time range from 6 to 24 h, which is likely due to the metabolism in tumor. These results reveal that DOX-HMPNs penetrate into the deep region of tumor and reach the highest accumulation at tumor sites at around 6 h after injection.

To further investigate the tumor-targeting performance of DOX-HMPNs, we carried out NIR fluorescence imaging *in vivo*. Prior to NIR fluorescence imaging, DOX-HMPNs were made fluorescent in the NIR region *via* the encapsulation of Cy5 (a widely used NIR fluorescent probe). After that, the MCF-7 tumor-bearing mice were intravenously injected with the free Cy5 and DOX-HMPNs^{Cy5} with equivalent Cy5 concentration, and the NIR fluorescence images were acquired at pre-designed time points (Fig. 5B and S18). Strong Cy5 fluorescence signal was found in tumor regions of DOX-HMPNs^{Cy5} group within 4 h, and this signal maintained up to at 24 h. Contrarily, a majority of fluorescence signal was distributed in the liver for the free Cy5 group. Moreover, the DOX-HMPNs^{Cy5} group showed much stronger fluorescence at tumor sites compared with the free Cy5 even at 24 h post-injection.

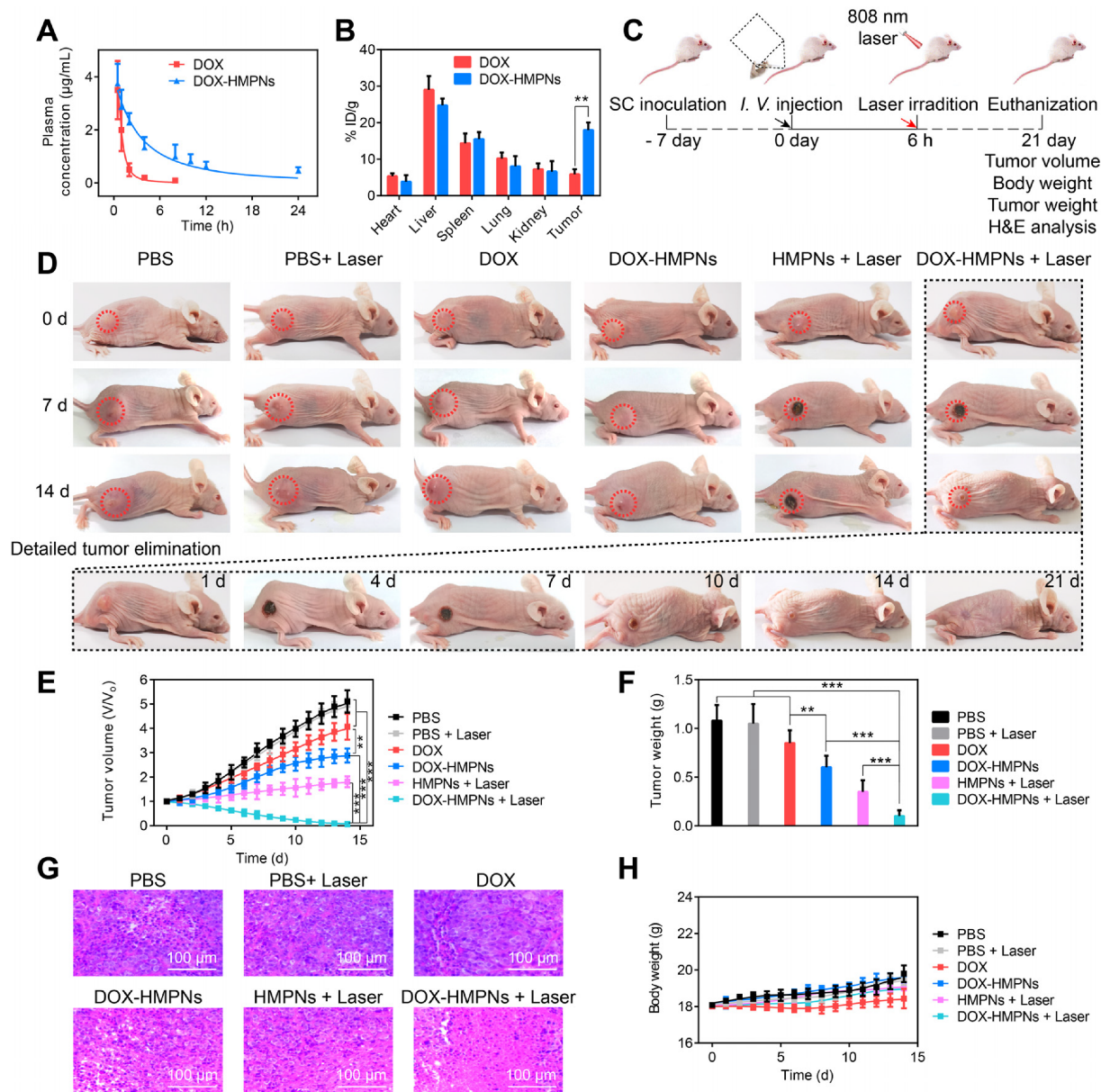


Fig. 6. (A) *In vivo* pharmacokinetic curve and (B) biodistribution of free DOX and DOX-HMPNs ($n = 3$). (C) Illustration of different antitumor treatments ($n = 4$). (D) Photographs of representative mice during different treatments. (E–H) Tumor growth curves of mice, excised tumor weight, representative H&E staining analysis of tumor tissues, and body weight changes of mice, respectively. Data were presented as mean \pm standard error. ** $P < 0.01$, *** $P < 0.005$.

These results indicate the excellent passive tumor-targeting ability of DOX-HMPNs. The tumor and healthy organs of mice were dissected to prove the biodistribution of DOX-HMPNs at 24 h post-injection (Fig. 5C,D and S19). For the free Cy5 group, evident fluorescence signal was distributed in the liver while weak fluorescence signal was observed to tumor tissues. In the case of DOX-HMPNs^{Cy5} group, the fluorescence signal was enriched at the tumor sites. CLSM images obtained from fresh-frozen tumor sections indicated the efficient accumulation of HMPNs in tumor tissues (Figure S20). Probably, the DOX-HMPNs preferentially accumulate in tumor regions via the considerable passive tumor-targeting.

Based on the *in vitro* photothermal and tumor-targeting abilities of the DOX-HMPNs, we further evaluated the *in vivo* photothermal performance by using MCF-7-bearing BALB/c mice. After intravenously injecting with DOX-HMPNs for 6 h, the *in vivo* photothermal images of the mice were acquired using thermal imaging to record the temperature evolution in tumor region (Fig. 5E and S21). The tumor local temperature of PBS group was just increased to ~ 38 °C upon the NIR laser irradiation (808 nm, 1 W cm⁻²) within 5 min. Under the same condition, the tumor local temperature of DOX-HMPNs group dramatically increased to ~ 57 °C. This effect can not only kill the cancer cells by photothermal therapy, but also realize the enhanced photothermal-chemotherapy, which further confirms the excellent *in vivo* photothermal performance as well as highly effective tumor accumulation of DOX-HMPNs. The same photothermal effect can be achieved by reducing the laser irradiation power while increasing the administration dose (Figure S22-24).

To confirm whether the HMPNs have the ability to prolong circulation life of DOX, we have conducted *in vivo* pharmacokinetic study through intravenous injection of free DOX and DOX-HMPNs into mice. As shown in Fig. 6A, the plasma concentration of DOX-HMPNs-injected mice is higher than that injected with free DOX. The plasma concentration of free DOX decreases rapidly and becomes undetectable after 8 h. However, DOX-HMPNs can be retained in bloodstream over 24 h. The mice were then euthanized and the biodistributions of the nanoparticles in major organs and tumors were measured by high performance liquid chromatography (HPLC) analysis. From Fig. 6B, the distribution of DOX-HMPNs in liver is much lower than that of free DOX. This result indicates that the *in situ* loading of DOX within HMPNs reduces the drug uptake by RES. DOX-HMPNs show significantly higher enrichment in tumor than the DOX. This is benefited from the negative surface charge of HMPNs, which prolongs their retention time during blood circulation and thus facilitates the efficient accumulation at tumor sites.

The BALB/c nude mice with MCF-7 tumor were separated into six groups ($n = 4$ per group): (1) PBS, (2) PBS with NIR laser irradiation, (3) DOX, (4) DOX-HMPNs (single chemotherapy), (5) HMPNs with NIR laser irradiation (single photothermal therapy), (6) DOX-HMPNs with NIR laser irradiation (photothermal-chemotherapy). Various formulations were intravenously injected into mice at a dosage of 3 mg DOX/kg, and the tumors were irradiated by using NIR laser (808 nm, 1 W cm⁻²) at 6 h post-injection (Fig. 6C). The representative photographs of mice, tumor volume change profiles and tumor weight are presented in Fig. 6D-F. The tumor volumes in PBS-treated group with and without irradiation exhibit a rapid increase over 21 days. The DOX-treated mice and DOX-HMPNs-treated mice without irradiation display a certain of delay in tumor growth due to DOX-mediated chemotherapy alone. HMPNs-treated mice with irradiation exhibit obvious tumor suppress, due to the HMPNs-mediated photothermal therapy alone. Significantly, the tumors of DOX-HMPNs-treated mice with irradiation shrink remarkably compared with the other groups and the tumors from 50% of mice were completely eliminated at the 21th day, due to the synergy of chemotherapy and photothermal therapy. The hematoxylin and eosin (H&E) staining of tumor sections indicate that the mice treated with DOX-HMPNs by combing with laser irradiation can achieve the most severe tumor cell destruction with the lowest viable

cell density in tumor tissues compared with the other groups (Fig. 6G). Besides, the body weight of all groups show no significant change during 21 days (Fig. 6H), and H&E staining of major organ sections in all groups exhibit no obvious signals of inflammation and cell death (Figure S25). These results imply the excellent photothermal-chemotherapy of DOX-HMPNs. During photothermal therapy, the heating induced by NIR irradiation would promote the drug uptake and intracellular delivery efficiency (see Fig. 4G) by enhancing cell membrane permeability and accelerating drug release (Fig. 3I). Therefore, the incomplete eradication of cancer cells by PTT alone could be nicely solved by this combination of chemotherapy and photothermal therapy [55–58].

3. Conclusion

In summary, we have developed a controllable method based on Kirkendall effect to fabricate HMPNs from boronate polymer nanospheres, which can facily encapsulate DOX (a model drug) to form DOX-HMPNs complex. The shell of HMPNs is composed of Fe^{III}/TAC coordination cross-linked polymer network, which has excellent absorption in NIR region and displays unique photoacoustic and photothermal properties. NIR laser (808 nm, 1 W cm⁻²) irradiation on a water dispersion of DOX-HMPNs (100 µg/mL) leads to almost 35.8 °C increase of temperature within 300 s, as well as causes intensive PA signal. Along with the dynamic Fe^{III}/TAC coordination, the HMPNs shell also comprises ionizable phenolic hydroxyl and cleavable imine bond, thus resulting in a programmable cascade response property. It has been observed that DOX-HMPNs can undergo a self-charge generation behavior and exhibit reversible “negative-to-positive” charge evolution in response to TME. Also, effective release of DOX can be achieved in the tumor cells with the cleavage of imine bond. By taking together the features of cascade response, photoacoustic imaging, and photothermal-chemotherapy, the as designed DOX-HMPNs show promising potential in targeted tumor synergistic theranostic. From the perspective of material design, the widely designable building blocks, selectable transition metal ions, and the highly adaptable etching method make this Kirkendall effect based strategy very interesting in the fabrication of other functional hollow nanomaterials.

Declaration of Competing Interest

The authors declare that they have no known competing financial interests or personal relationships that could have appeared to influence the work reported in this paper.

Acknowledgments

This work was supported by the National Natural Science Foundation of China (51673161, 51773172); Natural Science Foundation of Fujian Province (2019 J01032); Scientific and Technological Innovation Platform of Fujian Province (2014H2016); Science and Technology Major Project of the Fujian Province (2018HZ0001-1), the Project of National Key Research and Development Program (2019YFC0408505), the Key Research and Development Plan of Anhui Province (201904a07020070).

Appendix A. Supplementary data

Supplementary data to this article can be found online at <https://doi.org/10.1016/j.cej.2020.126690>.

References

- [1] S.S. Lucky, K.C. Soo, Y. Zhang, Nanoparticles in Photodynamic Therapy, *Chem. Rev.* 115 (4) (2015) 1990–2042.
- [2] W. Fan, B. Yung, P. Huang, X. Chen, *Nanotechnology for Multimodal Synergistic*

- Cancer Therapy, *Chem. Rev.* 117 (22) (2017) 13566–13638.
- [3] G. Tian, X. Zhang, Z. Gu, Y. Zhao, Recent Advances in Upconversion Nanoparticles-Based Multifunctional Nanocomposites for Combined Cancer Therapy, *Adv. Mater.* 27 (47) (2015) 7692–7712.
- [4] M.K. Yu, Y.Y. Jeong, J. Park, S. Park, J.W. Kim, J.J. Min, K. Kim, S. Jon, Drug-Loaded Superparamagnetic Iron Oxide Nanoparticles for Combined Cancer Imaging and Therapy in Vivo, *Angew. Chem. Int. Ed. Engl.* 47 (29) (2008) 5362–5365.
- [5] Q. Pei, X. Hu, X. Zheng, S. Liu, Y. Li, X. Jing, Z. Xie, Light-Activatable Red Blood Cell Membrane-Camouflaged Dimeric Prodrug Nanoparticles for Synergistic Photodynamic/Chemotherapy, *ACS Nano* 12 (2) (2018) 1630–1641.
- [6] R.H. Deng, M.Z. Zou, D. Zheng, S.Y. Peng, W. Liu, X.F. Bai, H.S. Chen, Y. Sun, P.H. Zhou, X.Z. Zhang, Nanoparticles from Cuttlefish Ink Inhibit Tumor Growth by Synergizing Immunotherapy and Photothermal Therapy, *ACS Nano* 13 (8) (2019) 8618–8629.
- [7] Y. Liu, P. Bhattarai, Z. Dai, X. Chen, Photothermal Therapy and Photoacoustic Imaging via Nanotheranostics in Fighting Cancer, *Chem. Soc. Rev.* 48 (7) (2019) 2053–2108.
- [8] G. Yang, L. Xu, Y. Chao, J. Xu, X. Sun, Y. Wu, R. Peng, Z. Liu, Hollow MnO₂ as a Tumor-Microenvironment-Responsive Biodegradable Nano-Platform for Combination Therapy Favoring Antitumor Immune Responses, *Nat. Commun.* 8 (1) (2017) 902–914.
- [9] J. Wang, J. Li, J. Yu, H. Zhang, B. Zhang, Large Hollow Cavity Luminous Nanoparticles with Near-Infrared Persistent Luminescence and Tunable Sizes for Tumor Afterglow Imaging and Chemo-/Photodynamic Therapies, *ACS Nano* 12 (5) (2018) 4246–4258.
- [10] X. Du, C. Zhao, M. Zhou, T. Ma, H. Huang, M. Jaroniec, X. Zhang, S.Z. Qiao, Hollow Carbon Nanospheres with Tunable Hierarchical Pores for Drug, Gene, and Photothermal Synergistic Treatment, *Small* 13 (6) (2017) 1602592–1602602.
- [11] R. Lv, P. Yang, F. He, S. Gai, G. Yang, J. Lin, Hollow Structured Y₂O₃:Yb/Er-CuxS Nanospheres with Controllable Size for Simultaneous Chemo/Photothermal Therapy and Bioimaging, *Chem. Mater.* 27 (2) (2015) 483–496.
- [12] W. Chen, K. Zeng, H. Liu, J. Ouyang, L. Wang, Y. Liu, H. Wang, L. Deng, Y.-N. Liu, Cell Membrane Camouflaged Hollow Prussian Blue Nanoparticles for Synergistic Photothermal-/Chemotherapy of Cancer, *Adv. Funct. Mater.* 27 (11) (2017) 1605795–1605803.
- [13] Q. Yu, Y. Han, X. Wang, C. Qin, D. Zhai, Z. Yi, J. Chang, Y. Xiao, C. Wu, Copper Silicate Hollow Microspheres-Incorporated Scaffolds for Chemo-Photothermal Therapy of Melanoma and Tissue Healing, *ACS Nano* 12 (3) (2018) 2695–2707.
- [14] Z. Dong, L. Feng, Y. Hao, M. Chen, M. Gao, Y. Chao, H. Zhao, W. Zhu, J. Liu, C. Liang, Q. Zhang, Z. Liu, Synthesis of Hollow Biomimetic CaCO₃-Polydopamine Nanoparticles for Multimodal Imaging-Guided Cancer Photodynamic Therapy with Reduced Skin Photosensitivity, *J. Am. Chem. Soc.* 140 (6) (2018) 2165–2178.
- [15] D. Xu, C. Zhou, C. Zhan, Y. Wang, Y. You, X. Pan, J. Jiao, R. Zhang, Z. Dong, W. Wang, X. Ma, Enzymatic Micromotors as a Mobile Photosensitizer Platform for Highly Efficient On-Chip Targeted Antibacteria Photodynamic Therapy, *Adv. Funct. Mater.* 29 (17) (2019) 1807727–1807737.
- [16] W.P. Li, C.H. Su, Y.C. Chang, Y.J. Lin, C.S. Yeh, Ultrasound-Induced Reactive Oxygen Species Mediated Therapy and Imaging Using a Fenton Reaction Activable Polymersome, *ACS Nano* 10 (2) (2016) 2017–2027.
- [17] M. Zhang, L. Zhang, Y. Chen, L. Li, Z. Su, C. Wang, Precise Synthesis of Unique Polydopamine/Mesoporous Calcium Phosphate Hollow Janus Nanoparticles for Imaging-Guided Chemo-Photothermal Synergistic Therapy, *Chem. Sci.* 8 (12) (2017) 8067–8077.
- [18] X. Chen, Q. Zhang, J. Li, M. Yang, N. Zhao, F.J. Xu, Rattle-Structured Rough Nanocapsules with in-Situ-Formed Gold Nanorod Cores for Complementary Gene/Chemo/Photothermal Therapy, *ACS Nano* 12 (6) (2018) 5646–5656.
- [19] Y. Li, G.H. Liu, J.Y. Ma, J.Y. Lin, H.R. Lin, G.H. Su, D.Y. Chen, S.F. Ye, X.Y. Chen, X. Zhu, Z.Q. Hou, Chemotherapeutic drug-photothermal agent co-self-assembling nanoparticles for near-infrared fluorescence and photoacoustic dual-modal imaging-guided chemo-photothermal synergistic therapy, *J. Controlled Release* 258 (2017) 95–107.
- [20] C. Ji, Q. Gao, X. Dong, W. Yin, Z. Gu, Z. Gan, Y. Zhao, M. Yin, A Size-Reducible Nanodrug with an Aggregation-Enhanced Photodynamic Effect for Deep Chemo-Photodynamic Therapy, *Angew. Chem. Int. Ed. Engl.* 57 (35) (2018) 11384–11388.
- [21] Y. Jang, S. Kim, S. Lee, C.M. Yoon, I. Lee, J. Jang, Graphene Oxide Wrapped SiO₂/TiO₂ Hollow Nanoparticles Loaded with Photosensitizer for Photothermal and Photodynamic Combination Therapy, *Chemistry* 23 (15) (2017) 3719–3727.
- [22] Y. Chang, Y. Cheng, Y. Feng, H. Jian, L. Wang, X. Ma, X. Li, H. Zhang, Resonance Energy Transfer-Promoted Photothermal and Photodynamic Performance of Gold-Copper Sulfide Yolk-Shell Nanoparticles for Chemophototherapy of Cancer, *Nano Lett.* 18 (2) (2018) 886–897.
- [23] S. Goel, C.A. Ferreira, F. Chen, P.A. Ellison, C.M. Siamof, T.E. Barnhart, W. Cai, Activatable Hybrid Nanotheranostics for Tetramodal Imaging and Synergistic Photothermal/Photodynamic Therapy, *Adv. Mater.* 30 (6) (2018) 1704367–1704375.
- [24] J. Li, Y. Hu, Y. Hou, X. Shen, G. Xu, L. Dai, J. Zhou, Y. Liu, K. Cai, Phase-Change Material Filled Hollow Magnetic Nanoparticles for Cancer Therapy and Dual Modal Bioimaging, *Nanoscale* 7 (19) (2015) 9004–9012.
- [25] H. Wang, Y. Sun, J. Yi, J. Fu, J. Di, A. del Carmen Alonso, S. Zhou, Fluorescent Porous Carbon Nanocapsules for Two-Photon Imaging, NIR/pH Dual-Responsive Drug Carrier, and Photothermal Therapy, *Biomaterials* 53 (2015) 117–126.
- [26] L. Dai, X. Li, X. Duan, M. Li, P. Niu, H. Xu, K. Cai, H. Yang, A pH/ROS Cascade-Responsive Charge-Reversal Nanosystem with Self-Amplified Drug Release for Synergistic Oxidation-Chemotherapy, *Adv. Sci.* 6 (4) (2019) 1801807–1801819.
- [27] K. Hayashi, T. Maruhashi, W. Sakamoto, T. Yogo, Organic-Inorganic Hybrid Hollow Nanoparticles Suppress Oxidative Stress and Repair Damaged Tissues for Treatment of Hepatic Fibrosis, *Adv. Funct. Mater.* 28 (13) (2018) 1706332–1706341.
- [28] X.Q. Wang, M. Peng, C.X. Li, Y. Zhang, M. Zhang, Y. Tang, M.D. Liu, B.R. Xie, X.Z. Zhang, Real-Time Imaging of Free Radicals for Mitochondria-Targeting Hypoxic Tumor Therapy, *Nano Lett.* 18 (11) (2018) 6804–6811.
- [29] D.E. Discher, A. Eisenberg, Polymer Vesicles, *Science* 297 (5583) (2002) 967–973.
- [30] B.M. Discher, Y.Y. Won, D.S. Ege, J.C. Lee, F.S. Bates, D.E. Discher, D.A. Hammer, Polymersomes: Tough Vesicles Made from Diblock Copolymers, *Science* 284 (5417) (1999) 1143–1146.
- [31] F. Caruso, R.A. Caruso, H. Mohwald, Nanoengineering of Inorganic and Hybrid Hollow Spheres by Colloidal Templating, *Science* 282 (5391) (1998) 1111–1114.
- [32] Y.D. Yin, R.M. Rioux, C.K. Erdonmez, S. Hughes, G.A. Somorjai, A.P. Alivisatos, Formation of Hollow Nanocrystals through the Nanoscale Kirkendall Effect, *Science* 304 (5671) (2004) 711–714.
- [33] Y. Son, Y. Son, M. Choi, M. Ko, S. Chae, N. Park, J. Cho, Hollow Silicon Nanostructures via the Kirkendall Effect, *Nano Lett.* 15 (10) (2015) 6914–6918.
- [34] H.G. Yang, H.C. Zeng, Preparation of Hollow Anatase TiO₂ Nanospheres via Ostwald Ripening, *J. Phys. Chem. B* 108 (11) (2004) 3492–3495.
- [35] L. Yu, R. Han, X. Sang, J. Liu, M.P. Thomas, B.M. Hudak, A. Patel, K. Page, B.S. Gupton, Shell-Induced Ostwald Ripening: Simultaneous Structure, Composition, and Morphology Transformations during the Creation of Hollow Iron Oxide Nanocapsules, *ACS Nano* 12 (9) (2018) 9051–9059.
- [36] X. Xia, Y. Wang, A. Ruditskiy, Y. Xia, 25th Anniversary Article: Galvanic Replacement: a Simple and Versatile Route to Hollow Nanostructures with Tunable and Well-Controlled Properties, *Adv. Mater.* 25 (44) (2013) 6313–6333.
- [37] M. Hajfathalian, K.D. Gilroy, S.D. Golze, A. Yaghoubsade, E. Menemerov, R.A. Hughes, S. Neretina, A. Wulff in a Cage: The Confinement of Substrate-Based Structures in Plasmonic Nanoshells, Nanocages, and Nanoframes Using Galvanic Replacement, *ACS Nano* 10 (6) (2016) 6354–6362.
- [38] C. Yuan, T. Wu, J. Mao, T. Chen, Y. Li, M. Li, Y. Xu, B. Zeng, W. Luo, L. Yu, G. Zheng, L. Dai, Predictable Particle Engineering: Programming the Energy Level, Carrier Generation, and Conductivity of Core-Shell Particles, *J. Am. Chem. Soc.* 140 (24) (2018) 7629–7636.
- [39] C. Yuan, B. Hong, Y. Chang, J. Mao, Y. Li, Y. Xu, B. Zeng, W. Luo, J.F. Gerard, L. Dai, Cross-Linking Induced Self-Organization of Polymers into Degradable Assemblies, *ACS Appl. Mater. Interfaces* 9 (17) (2017) 14700–14708.
- [40] L.L. Dai, K. Li, M.H. Li, X.J. Zhao, Z. Luo, L. Lu, Y.F. Luo, K.Y. Cai, Size/Charge Changeable Acidity-Responsive Micelleplex for Photodynamic-Improved PD-L1 Immunotherapy with Enhanced Tumor Penetration, *Adv. Funct. Mater.* 28 (18) (2018) 1707249–1707264.
- [41] D. Pranantyo, P. Liu, W.B. Zhong, E.T. Kang, M.B. Chan-Park, Antimicrobial Peptide-Reduced Gold Nanoclusters with Charge-Reversal Moieties for Bacterial Targeting and Imaging, *Biomacromolecules* 20 (8) (2019) 2922–2933.
- [42] M.J. Sun, J. Li, C.T. Zhang, Y. Xie, H.Z. Qiao, Z.G. Su, D. Oupicky, Q.N. Ping, Arginine-Modified Nanostructured Lipid Carriers with Charge-Reversal and pH-Sensitive Membranolytic Properties for Anticancer Drug Delivery, *Adv. Healthc. Mater.* 6 (8) (2017) 1600693–1600704.
- [43] T. Shen, S.L. Guan, Z.H. Gan, G. Zhang, Q.S. Yu, Polymeric Micelles with Uniform Surface Properties and Tunable Size and Charge: Positive Charges Improve Tumor Accumulation, *Biomacromolecules* 17 (5) (2016) 1801–1810.
- [44] Y.Y. Yuan, C.Q. Mao, X.J. Du, J.Z. Du, F. Wang, J. Wang, Surface Charge Switchable Nanoparticles Based on Zwitterionic Polymer for Enhanced Drug Delivery to Tumor, *Adv. Mater.* 24 (40) (2012) 5476–5480.
- [45] F. You, Y. Xu, X. Yang, Y. Zhang, L. Shao, Bio-Inspired Ni²⁺-Polyphenol Hydrophilic Network to Achieve Unconventional High-Flux Nanofiltration Membranes for Environmental Remediation, *Chem. Commun.* 53 (45) (2017) 6128–6131.
- [46] S. Kim, T. Gim, S.M. Kang, Stability-Enhanced Polydopamine Coatings on Solid Substrates by Iron(III) Coordination, *Prog. Org. Coat.* 77 (8) (2014) 1336–1339.
- [47] S.B. Jin, J.P. Hill, Q.M. Ji, L.K. Shrestha, K. Ariga, Supercapacitive Hybrid Materials from the Thermolysis of Porous Coordination Nanorods Based on a Catechol Porphyrin, *J. Mater. Chem. A* 4 (15) (2016) 5737–5744.
- [48] J.T. Weisser, M.J. Nilges, M.J. Sever, J.J. Wilker, EPR Investigation and Spectral Simulations of Iron-Catecholate Complexes and Iron-Peptide Models of Marine Adhesive Cross-Links, *Inorg. Chem.* 45 (19) (2006) 7736–7747.
- [49] M.J. Sever, J.T. Weisser, J. Monahan, S. Srinivasan, J.J. Wilker, Metal-Mediated Cross-Linking in the Generation of a Marine-Mussel Adhesive, *Angew. Chem. Int. Ed.* 43 (4) (2004) 448–450.
- [50] P. Zhang, Y. Hou, J. Zeng, Y. Li, Z. Wang, R. Zhu, T. Ma, M. Gao, Coordinatively Unsaturated Fe³⁺ Based Activable Probes for Enhanced MRI and Therapy of Tumors, *Angew. Chem. Int. Ed.* 58 (32) (2019) 11088–11096.
- [51] T. Liu, W. Liu, M. Zhang, W. Yu, F. Gao, C. Li, S.B. Wang, J. Feng, X.Z. Zhang, Ferrous-Supply-Regeneration Nanoengineering for Cancer-Cell-Specific Ferroptosis in Combination with Imaging-Guided Photodynamic Therapy, *ACS Nano* 12 (12) (2018) 12181–12192.
- [52] J. Mao, Y. Li, T. Wu, C. Yuan, B. Zeng, Y. Xu, L. Dai, A Simple Dual-pH Responsive Prodrug-Based Polymeric Micelles for Drug Delivery, *ACS Appl. Mater. Interfaces* 8 (27) (2016) 17109–17117.
- [53] L. Qiu, C.Y. Hong, C.Y. Pan, Doxorubicin-Loaded Aromatic Imine-Contained Amphiphilic Branched Star Polymer Micelles: Synthesis, Self-Assembly, and Drug Delivery, *Int. J. Nanomedicine* 10 (2015) 3623–3640.
- [54] S.N. Yang, F.Y. Zhu, Q. Wang, F.X. Liang, X.Z. Qu, Z.H. Gan, Z.Z. Yang, Combinatorial Targeting Polymeric Micelles for Anti-Tumor Drug Delivery, *J. Mater. Chem. B* 3 (19) (2015) 4043–4051.
- [55] Y. Li, J. Lin, P. Wang, Q. Luo, H. Lin, Y. Zhang, Z. Hou, J. Liu, X. Liu, Tumor Microenvironment Responsive Shape-Reversal Self-Targeting Virus-Inspired Nanodrug for Imaging-Guided Near-Infrared-II Photothermal Chemotherapy, *ACS*

- Nano 13 (11) (2019) 12912–12928.
- [56] Y. Xu, J. Chen, L. Tong, P. Su, Y. Liu, B. Gu, B. Bao, L. Wang, pH/NIR-Responsive Semiconducting Polymer Nanoparticles for Highly Effective Photoacoustic Image Guided Chemo-Photothermal Synergistic Therapy, *Journal of Controlled Release* 293 (2019) 94–103.
- [57] F. Yu, M. Zhu, N. Li, M. Ao, Y. Li, M. Zhong, Q. Yuan, H. Chen, Z. Fan, Y. Wang, Z. Hou, Z. Qi, Y. Shen, X.D. Chen, Imaging-Guided Synergistic Targeting-Promoted Photo-Chemotherapy Against Cancers by Methotrexate-Conjugated Hyaluronic Acid Nanoparticles, *Chemical Engineering Journal* 380 (2020) 122426–122438.
- [58] Z. Li, J. Liu, Y. Hu, K.A. Howard, Z. Li, X. Fan, M. Chang, Y. Sun, F. Besenbacher, C. Chen, M. Yu, Multimodal Imaging-Guided Antitumor Photothermal Therapy and Drug Delivery Using Bismuth Selenide Spherical-Sponge, *ACS Nano* 10 (1) (2016) 9646–9658.